

Supporting Information

Mesoporous TiO₂ Mesocrystals: Remarkable Defects-Induced Crystallite-Interface Reactivity and Their *in-situ* Conversion to Single-Crystals

Yong Liu¹, Yongfeng Luo^{1,2}, Ahmed A. Elzatahry^{3,4}, Wei Luo^{1,5}, Renchao Che¹, Jianwei Fan^{1,6}, Kun Lan¹, Abdullah M. Al-Enizi⁷, Zhenkun Sun¹, Bin Li¹, Zhengwang Liu¹, Dengke Shen¹, Yun Ling¹, Chun Wang¹, Jingxiu Wang¹, Wenjun Gao¹, Chi Yao¹, Kaiping Yuan¹, Huisheng Peng⁸, Yun Tang¹, Yonghui Deng¹, Gengfeng Zheng¹, Gang Zhou¹ & Dongyuan Zhao¹

¹ Department of Chemistry, Shanghai Key Laboratory of Molecular Catalysis and Innovative Materials, State Key Laboratory of Molecular Engineering of Polymers, Laboratory of Advanced Materials, Fudan University, Shanghai, 200433, China

² College of Science, Central South University of Forestry and Technology, Changsha, Hunan 410004, China

³ Materials Science and Technology Program, College of Arts and Sciences, Qatar University, P.O. Box 2713, Doha, Qatar

⁴ Polymer Materials Research Department, Advanced Technology and New Materials Research Institute, City of Scientific Research and Technology Applications, New Borg El-Arab City, Alexandria 21934, Egypt.

⁵ State Key Laboratory for Modification of Chemical Fibers and Polymer Materials, College of Materials Science and Engineering, Donghua University, Shanghai 201620, P. R. China

⁶ College of Environmental Science and Engineering, State Key Laboratory of Pollution Control and Resource Reuse, Tongji University, Shanghai 200092, P. R. China.

⁷ Department of Chemistry-College of Science, King Saud University, Riyadh 11451, Saudi Arabia.

⁸ State Key Laboratory of Molecular Engineering of Polymers, Department of Macromolecular Science, and Laboratory of Advanced Materials, Fudan University, Shanghai 200438, China.

E-mail: dyzhao@fudan.edu.cn

Homepage: <http://www.mesogroup.fudan.edu.cn/>

METHODS

Synthesis of mesoporous TiO₂ mesocrystals (FDU-19) and their derivative SC-FDU-19 and SN-FDU-19. The olive-shaped mesoporous TiO₂ mesocrystals FDU-19 were synthesized by an evaporation-driven oriented assembly (EDOA) approach in an acidic tetrahydrofuran (THF)/Pluronic F127/H₂O/HCl/Acetic acid (HOAc)/Titanium tetrabutoxide (TBOT) mixed solution. For a typical synthesis, 1.5 g of Pluronic F127 (PEO₁₀₆PPO₇₀PEO₁₀₆, Mw = 12,600 g/mol), 0.1 g of H₂O, 2.0 g of HOAc and 1.8 g of concentrated HCl (36 wt%) were dissolved in 30 ml of THF. The mixture was vigorously stirred for 30 min to form a transparent solution. Sequentially, 3.0 g of TBOT was added dropwise under vigorous stirring for 30 min to form a clear golden yellow solution. After that, the obtained solution was transferred into a volumetric flask, and left it in a drying oven to evaporate THF at 60 °C for 12 h to completely remove all the solvents. The milky white precipitate obtained was finally calcinated in a tubular furnace under N₂ at 350 °C for 2 h to obtain a uniform olive-shaped mesoporous TiO₂ mesocrystals FDU-19. The olive-shaped mesoporous anatase single-crystals (SC-FDU-19) could be obtained by annealing of the FDU-19 mesocrystals in air at 400 °C for 2 h. The ultrathin single-crystal anatase nanosheets (SN-FDU-19) could be obtained by annealing of FDU-19 mesocrystals in vacuum ($\sim 4.0 \times 10^{-5}$ Pa) at 400 °C for about 45 min.

Materials characterization. Transmission electron microscopy (TEM) experiments were conducted on a JEOL JEM-2100F (UHR) microscope (Japan) operated at 200 kV. *In-situ* TEM heating experiments were carried out on a grid with molybdenum supporting film using the EM-21130 Specimen Heating Holder. Field-emission scanning electron microscopy (FESEM) images were collected on the Hitachi Model S-4800 field-emission scanning electron microscope. To obtain information during the EDOA process, *cryo*-scanning electron microscopy (*cryo*-SEM) images were taken on the samples functioned with the evaporation time. Small amount of the reactant solution (about 0.1 mL) was withdrawn at different stages during the solvent evaporation. The solution was dropped on a concave copper sample holder and quickly emerged into a soil nitrogen (a kind of semisolid nitrogen made by treating liquid

nitrogen under vacuum) to form a solid specimen. The Electron paramagnetic resonance (EPR) spectra were recorded on a Bruker EPR spectrometer at an X-band frequency of 9.877 GHz, sweep width of 1000 Gauss, and center field of 3500 Gauss. X-ray diffraction (XRD) patterns were recorded with a Bruker D8 powder X-ray diffractometer (Germany) using Cu K α radiation (40 kV, 40 mA). Nitrogen sorption isotherms were measured at 77 K with a Micromeritics Tristar 3020 analyzer (USA). Synchrotron radiation small-angle X-ray scattering (SAXS) measurements were performed at Beamline BL16B of Shanghai Synchrotron Radiation Facility (SSRF). The *d*-spacing values were calculated from the formula $d = 2\pi/q$. Before measurements, the samples were degassed in a vacuum at 180 °C for at least 6 h. The Brunauer–Emmett–Teller (BET) method was utilized to calculate the specific surface areas. By using the Barrett-Joyner-Halenda (BJH) model, the pore volumes and pore size distributions were derived from the adsorption branches of isotherms. The Dynamic light scattering (DLS) and zeta potential (ζ) experiments were carried out on a Malvern Zetasizer 3600 (Malvern Instruments). The UV-Vis analysis was carried out by using a Shimadzu UV-2450 spectrophotometer from 200 to 800 nm. X-ray photoelectron spectroscopy (XPS) was recorded on an AXIS ULTRA DLD XPS System with MONO Al source (Shimadzu Corp.). Photoelectron spectrometer was recorded by using monochromatic Al K α radiation under vacuum at 5×10^{-9} Pa. All of the binding energies were referenced to the C $_{1s}$ peak at 284.6 eV of the surface adventitious carbon. Electrochemical impedance spectroscopy (EIS) was performed with a Zennium electrochemical workstation in a frequency range between 10 mHz and 1 MHz. The magnitude of the alternative signal was 10 mV. The impedance measurements were carried out under a forward bias of -0.80 V in the dark condition. The resulting impedance spectra were fitted with Z-view software.

Photovoltaic Measurements. To prepare dye-sensitized solar cells (DSSCs) working electrodes, 0.24 g of TiO $_2$ samples was first dispersed into a mixture containing 0.05 g of ethyl cellulose, 0.5 ml of terpinol and 0.15 ml of acetylacetone. The mixture was sonicated for 45 min to form a slurry. Then, the resultant slurry was coated on the fluorine-doped tin oxide (FTO) glass by screen printing

technology. The working electrode was heated to 450 °C for 30 min and annealed in air. It was then immersed in an aqueous solution of TiCl_4 (40 mM) at 70 °C for 30 min and washed with deionized water and ethanol, followed by sintering at 450 °C for 30 min. After the temperature decreased to 120 °C, it was immersed into a commercial N719 dye solution (0.3 mM) in dry acetonitrile and tertbutanol (1:1) for 16 h. The N719-incorporated electrodes were carefully rinsed with dry acetonitrile. The working and counter electrodes with a Surlyn frame as the spacer were sealed by pressing them together at a pressure of about 0.2 MPa and a temperature of 125 °C. The redox electrolyte (composed of 0.1 M lithium iodide, 0.05 M iodine, 0.6 M 1, 2-dimethyl-3-propyl-imidazolium iodide and 0.5 M 4-tert butyl-pyridine in dehydrated acetonitrile) was introduced into the cell through the back hole of the counter electrode. Finally, the hole was sealed with the Surlyn and a cover glass. A platinum counter electrode was prepared by coating H_2PtCl_6 onto FTO glass, followed by thermal decomposition at 500 °C in air for 30 min. The J–V characteristics were measured by a Keithley 2400 Source Meter under the illumination (100 mW/cm^2) of AM1.5 simulated solar light coming from a solar simulator (Oriel-Sol3A94023A equipped with a 450 W Xe lamp and an AM1.5 filter). The light intensity was calibrated by using a reference Si solar cell (Oriel-91150). A black metal mask with an aperture area of 0.16 cm^2 was attached to the device surface to avoid stray light during the measurements. For the DSSCs based on the FDU-19, SC-FDU-19 and P25, a white paper was placed below the device during the measurements. The incident photo-to-current conversion efficiencies (IPCE) spectra were measured with an Oriel-74125 system (Oriel Instruments, USA), where the intensity of monochromatic light was measured with a Si detector (Oriel-71640).

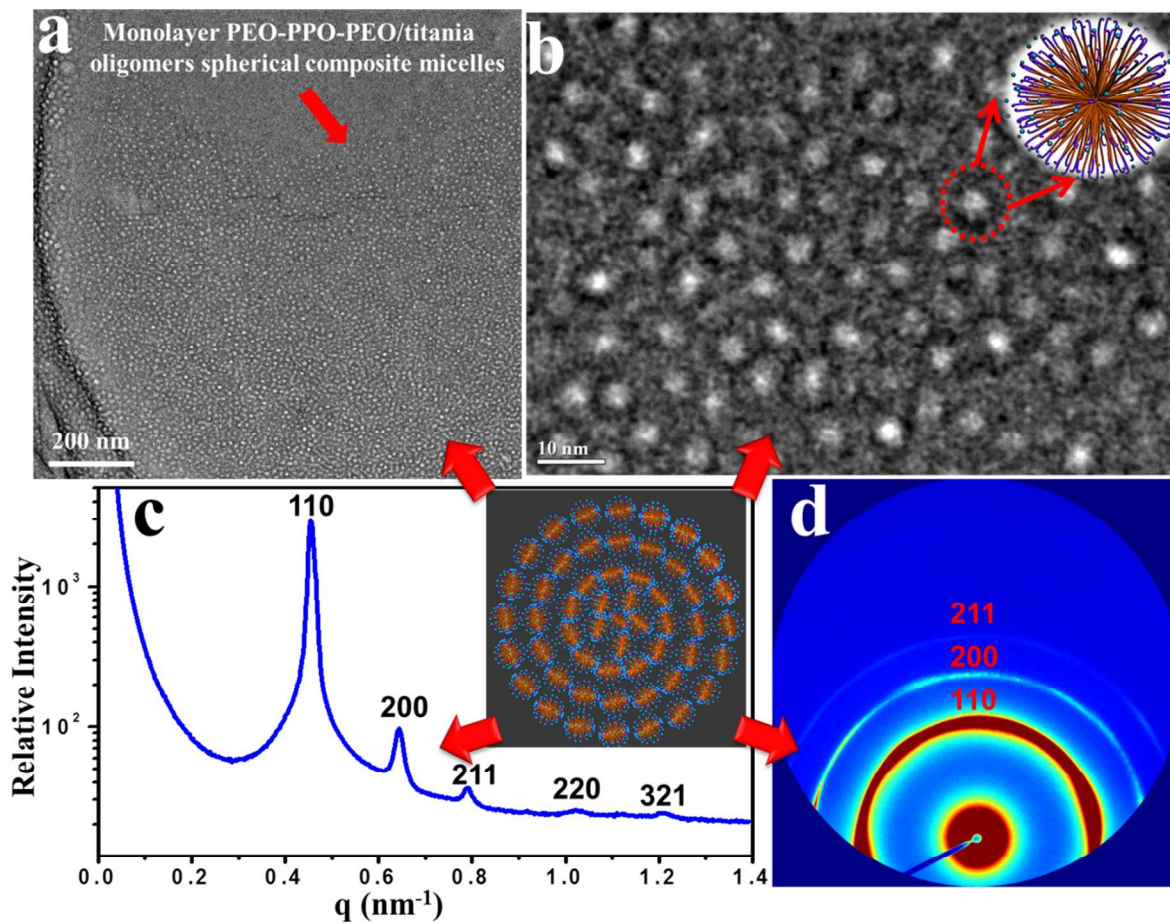


Figure S1. (a, b) TEM images and (c, d) synchrotron radiation SAXS patterns of the aqueous sample taken from the reaction solution after THF evaporation at 60 °C for 3 h. The white nanospheres in TEM images are the PEO-PPO-PEO spherical micelles and the tiny black dots are titania oligomers. The above TEM images and SAXS patterns clearly show that the spherical composite micelles are initially oriented in a 2D membrane form (cubic $Im\bar{3}m$ mesophase) at the interface between THF and water phases. The spherical micelles possess a typical core-shell structure with PEO-PPO-PEO as a core and titania oligomers as a shell.

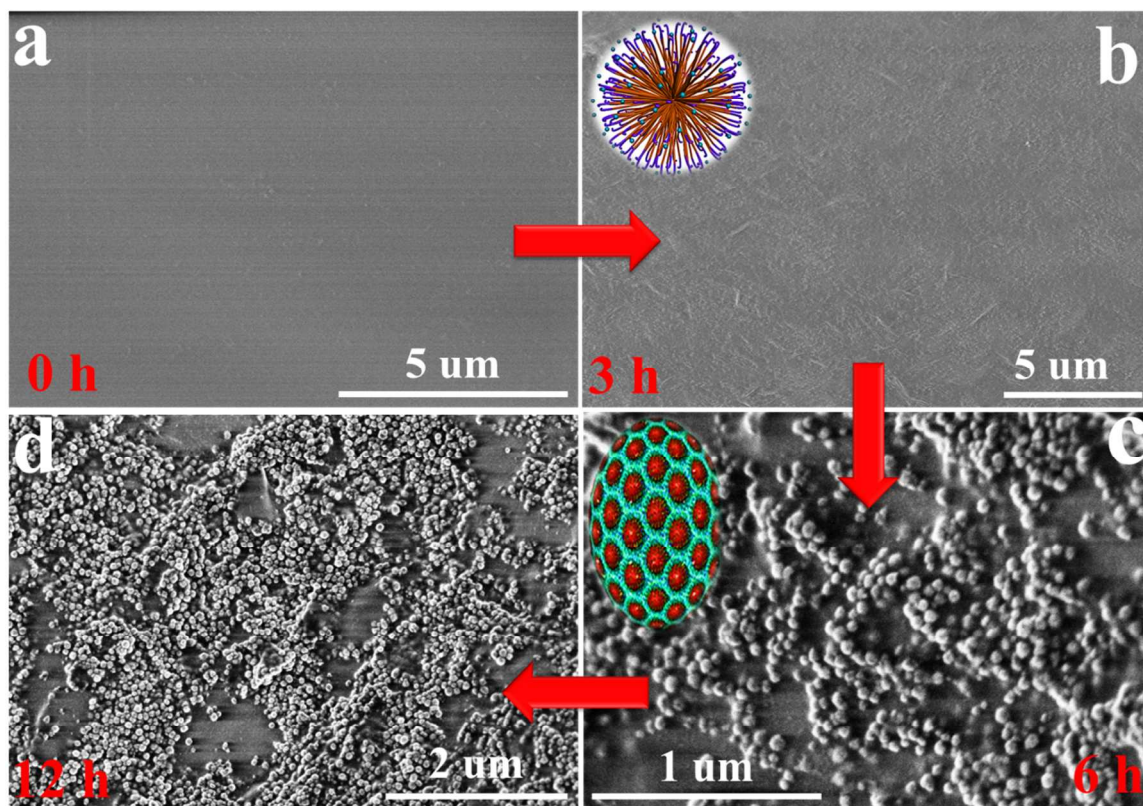


Figure S2. *Cryo*-SEM images of the samples harvested from THF/F127/H₂O/HCl/HOAc/TBOT mixed acidic solution at different intervals of time (a), 0 h, (b), 3 h, (c), 6 h and (d), 12 h.

To shed more light on the formation mechanism of the olive-shaped mesoporous TiO₂ mesocrystals (FDU-19), their growth process was followed by examining the products harvested at different intervals of time during the solvent evaporation. Before the electron microscopy analysis, the samples were frozen by soil nitrogen. The *cryo*-SEM image (Fig. S2b) shows that uniform spherical particles are well dispersed in the solution, suggesting that the spherical PEO-PPO-PEO/titania-oligomer composite micelles are firstly formed at the interface between the THF-rich and water-rich phases. As two solvents (THF and water) further evaporates for 6 h at 60 °C, the olive-shaped spherical particles (about 150 nm in size) are derived from the liquid-liquid interface (Fig. S2c), suggesting that the spherical composite micelles are spontaneously aggregated into the olive-like spheres at the high concentration of micelles and separated from the liquid phase. After these colloidal spheres are further dried at 60 °C for 12 h, the continuous evaporation of the residue THF and hydrolysed solvents (such as butanol) drives the oriented growth of both mesochannels and flake-like nanocrystal building blocks from the initially formed spherical composite micelles along the free radial and restricted tangential direction, yielding 3D-open olive-shaped mesoporous TiO₂ mesocrystals (Fig. S2d).

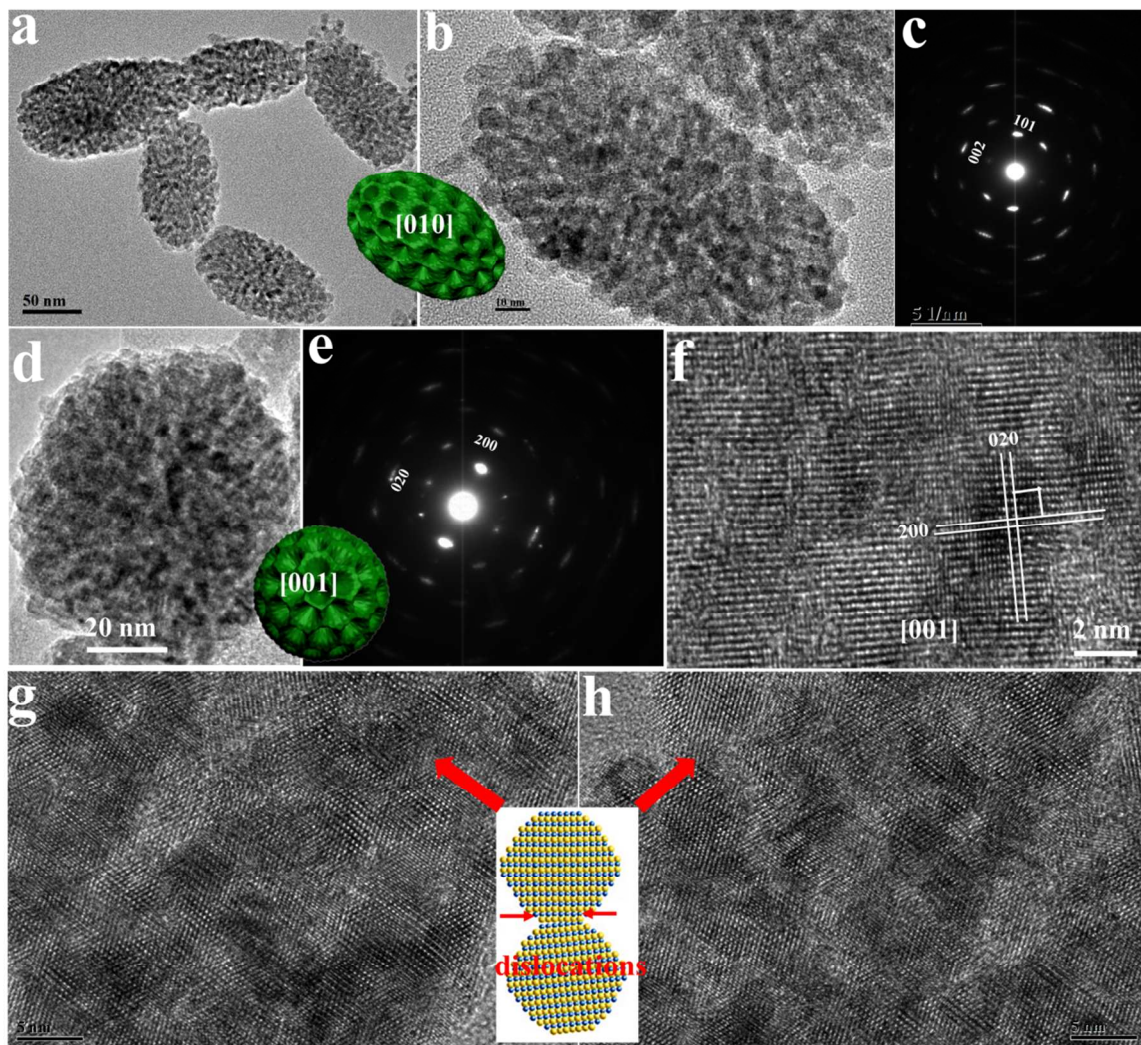


Figure S3. (a, b) TEM images of the mesoporous TiO_2 mesocrystals FDU-19, recorded along the [010] axis with different magnifications; (c) SAED patterns of an individual mesoporous TiO_2 mesocrystal FDU-19, recorded along the [010] axis. (d) TEM image of the mesoporous TiO_2 mesocrystals FDU-19, recorded along the [001] axis; (e), SAED patterns of an individual TiO_2 mesocrystal FDU-19, recorded along the [010] and [001] axis, respectively; (f, g, h) HRTEM images of an individual mesoporous TiO_2 mesocrystal FDU-19 recorded along [001] axis (f), [010] axis. The HRTEM images clearly reveal dislocations and edge defects between the adjacent flake-like nanocrystal building blocks. The SAED patterns taken along [010] and [001] show identical elongated diffraction spots.

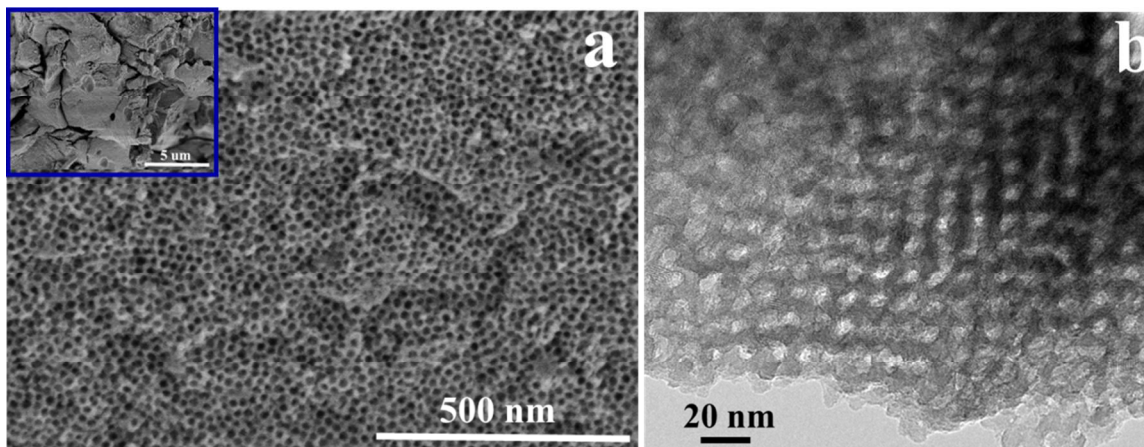


Figure S4. (a) SEM and (b) TEM image of the mesoporous TiO₂ bulks obtained with the aid of swelling 1,3,5-trimethylbenzene (TMB) molecules. Inset (a) is the overall morphology of the mesoporous TiO₂ bulks.

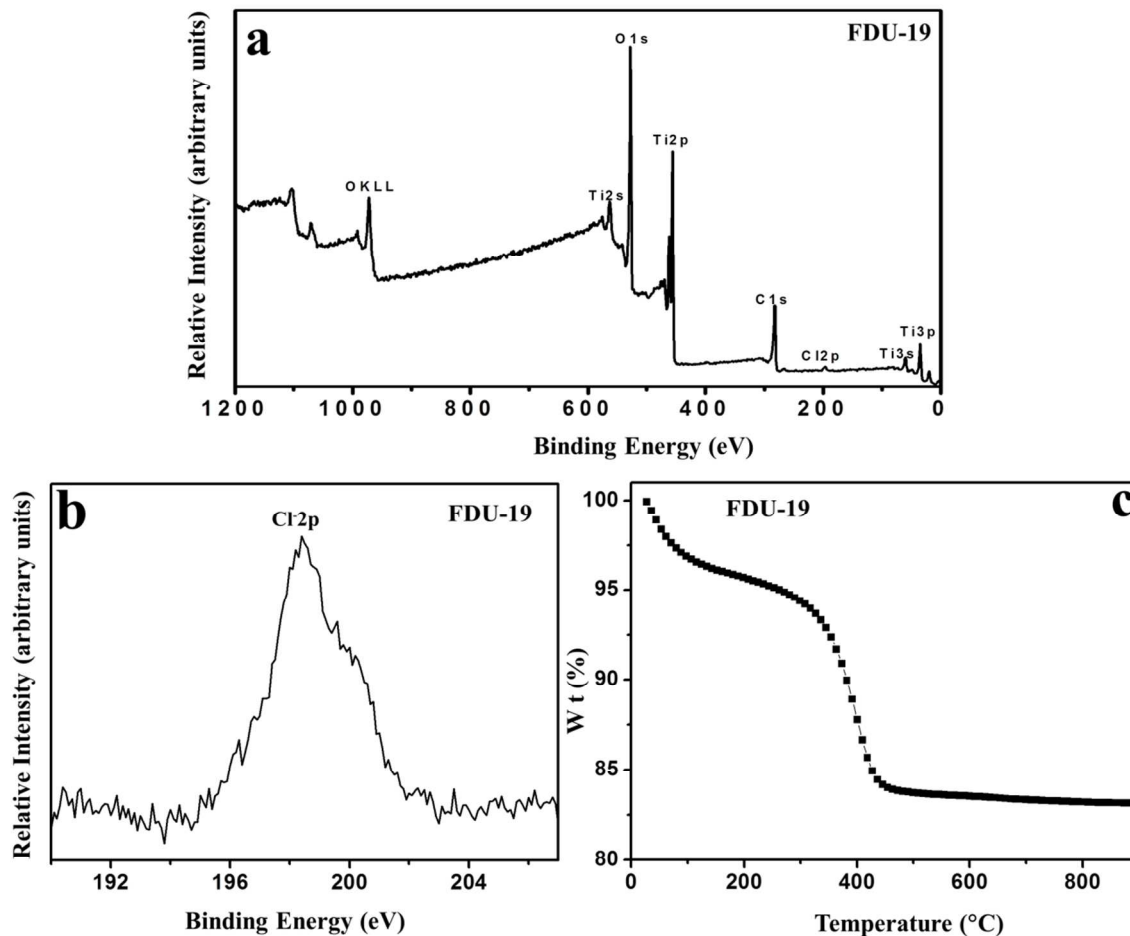


Figure S5. (a), The X-ray photoelectron spectra (XPS) of the mesoporous TiO₂ mesocrystals FDU-19, showing the three characteristic peaks of Ti, O and Cl. (b), Cl_{2p} XPS core-level spectra for FDU-19, indicating the adsorption of Cl⁻ on the surface. (c), The thermogravimetry (TG) curve of the FDU-19 mesocrystal particles conducted in air. The TG curve contains two main stages for weight loss. The first stage from room temperature to 200 °C with a mass loss of ~ 5 % is caused by dehydration from the surface of FDU-19. The second stage with ~ 10 % mass loss from 200 to 400 °C is attributed to the removal of chemisorbed hydroxyl groups (-OH), water on the FDU-19 mesocrystal particles.

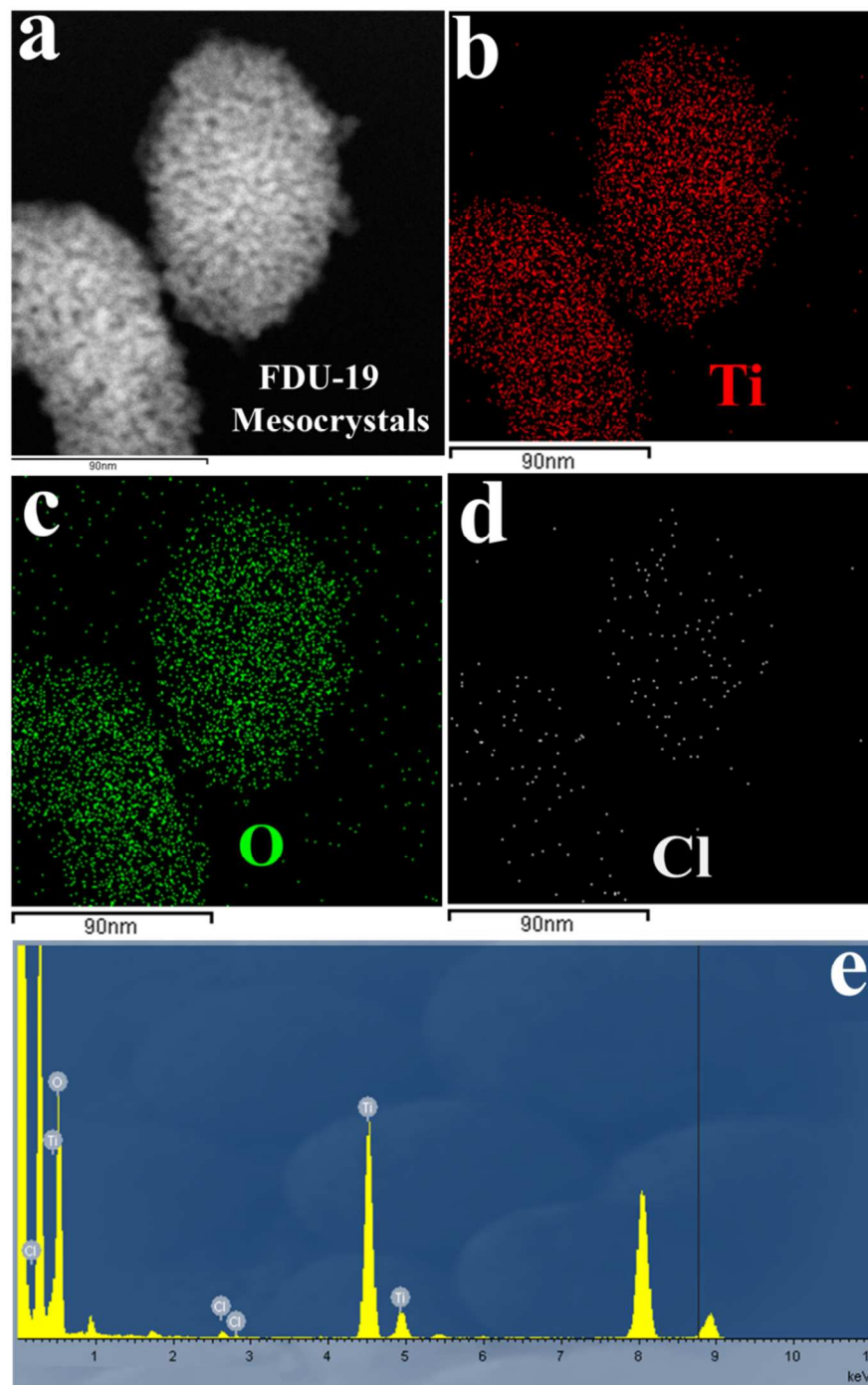


Figure S6. (a), The STEM image of a single mesoporous TiO_2 mesocrystal FDU-19 after calcination in N_2 at 350 °C for 2 h; (b-e), EDX elemental maps of Ti, O and Cl, respectively, for a single mesocrystal FDU-19, showing a small amount of Cl^- ions adsorption on the surface.

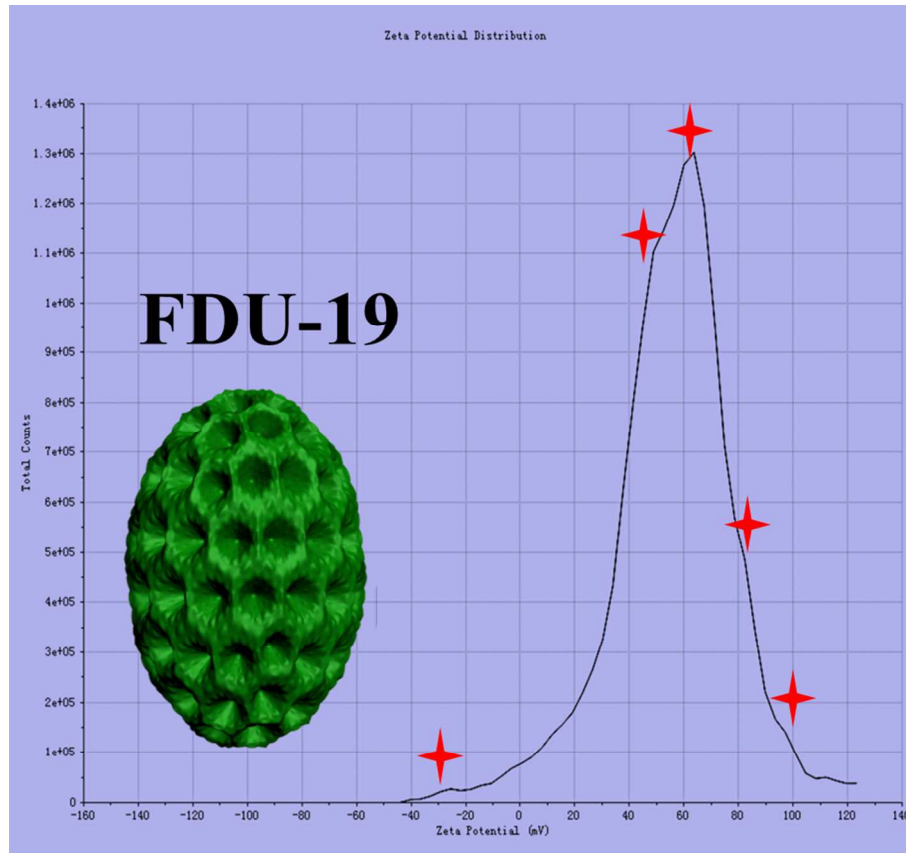


Figure. S7. Zeta potential value (ζ) of the mesoporous TiO₂ mesocrystals FDU-19 dispersed in water, showing the existence of mainly positive charges and a few negative charges.

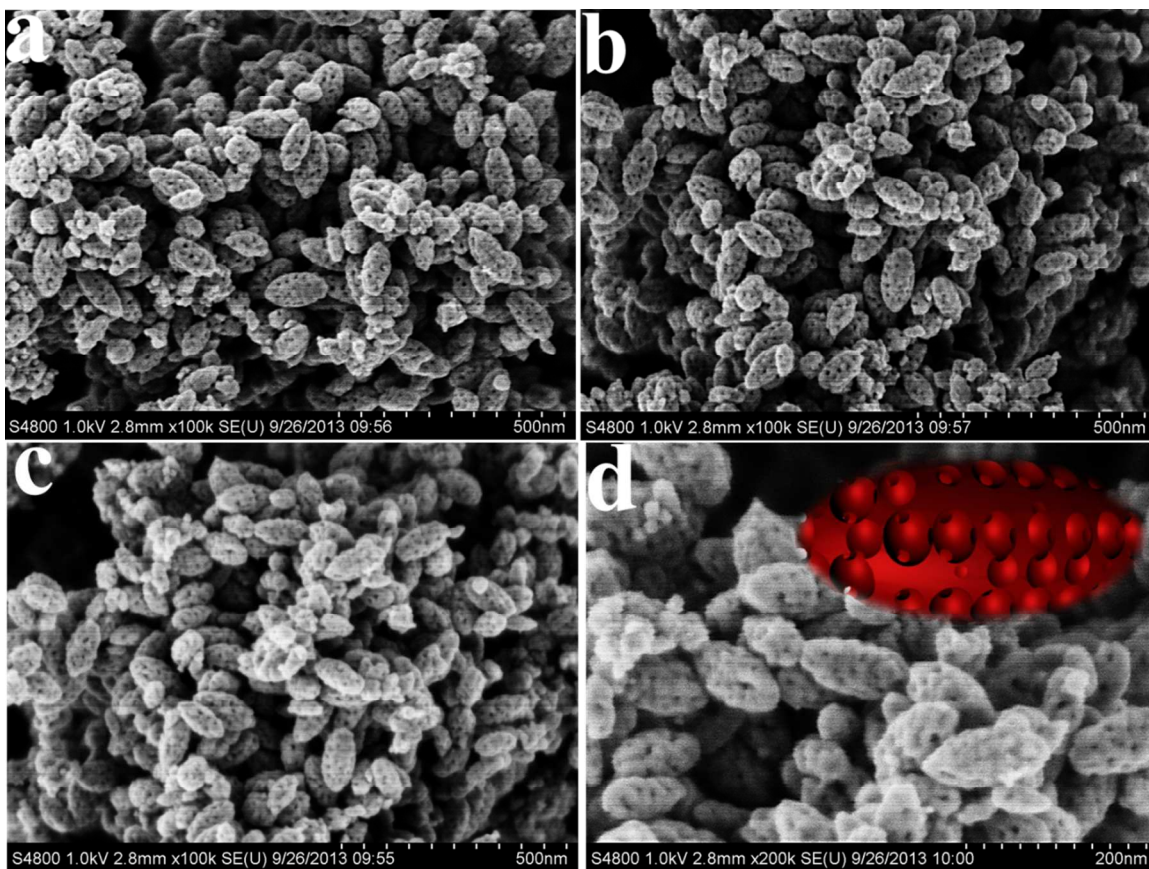


Figure S8. SEM images of the mesoporous TiO_2 single-crystals SC-FDU-19 after the calcination in air at $400\text{ }^\circ\text{C}$ for 2 h, showing that the annealing in air can drive a regular 3D *in-situ* fusion of the mesopore mesochannels of the mesocrystals FUD-19 into 3D open spherical mesopores. Inset (d) is the schematic illustration of the mesoporous TiO_2 single-crystals SC-FDU-19.

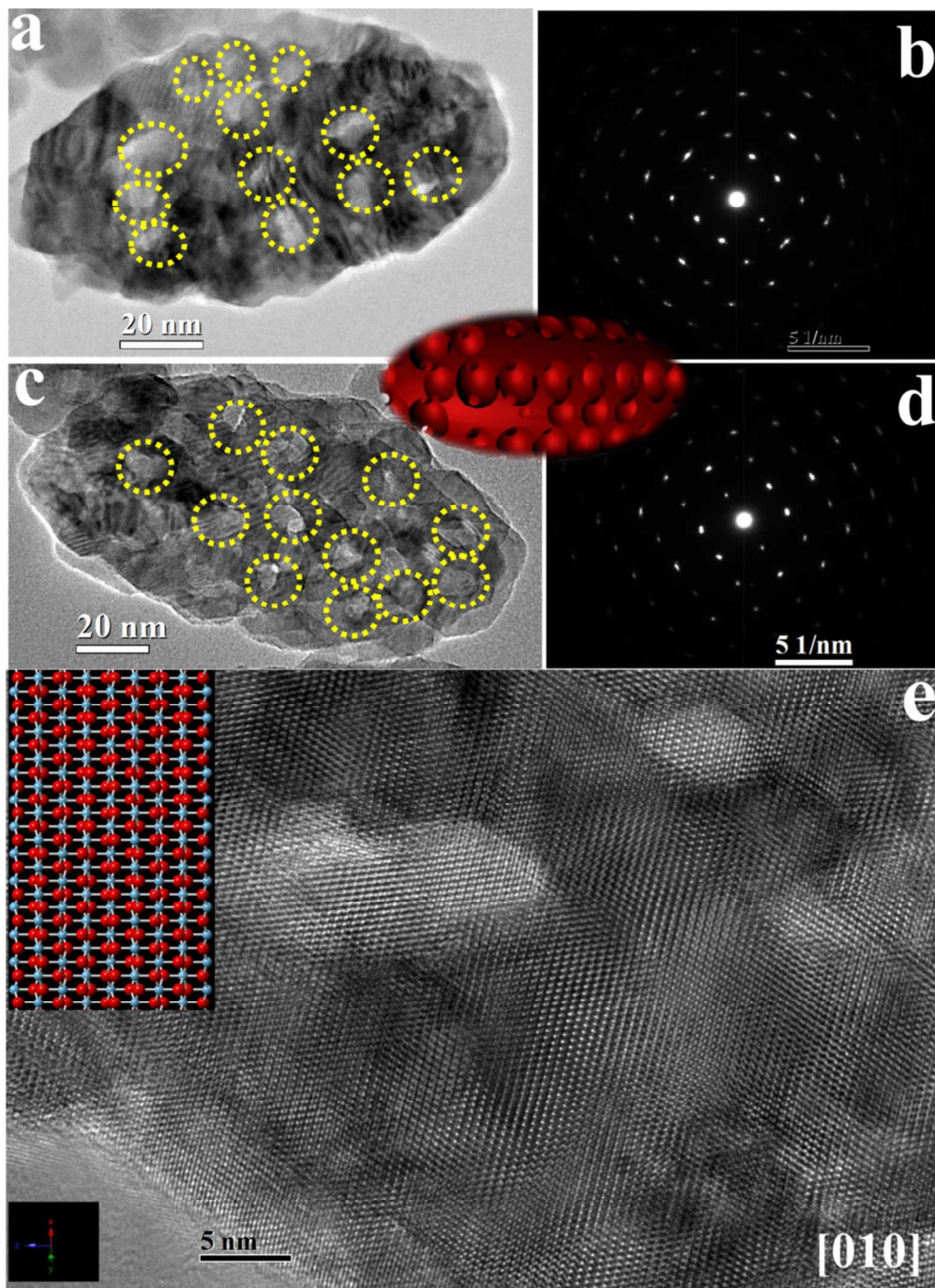


Figure S9. (a, c) TEM images and (b, d) SAED patterns of an individual mesoporous TiO_2 single-crystal particle SC-FDU-19; (e) HRTEM image of a single particle SC-FDU-19 recorded along [010] axis. Inset (e) is the corresponding crystallographic structure of the mesoporous TiO_2 single-crystals SC-FDU-19. Ti and O atoms are represented by blue and red spheres, respectively. The above TEM and SAED results clearly show the single-crystalline characteristic of SC-FDU-19.

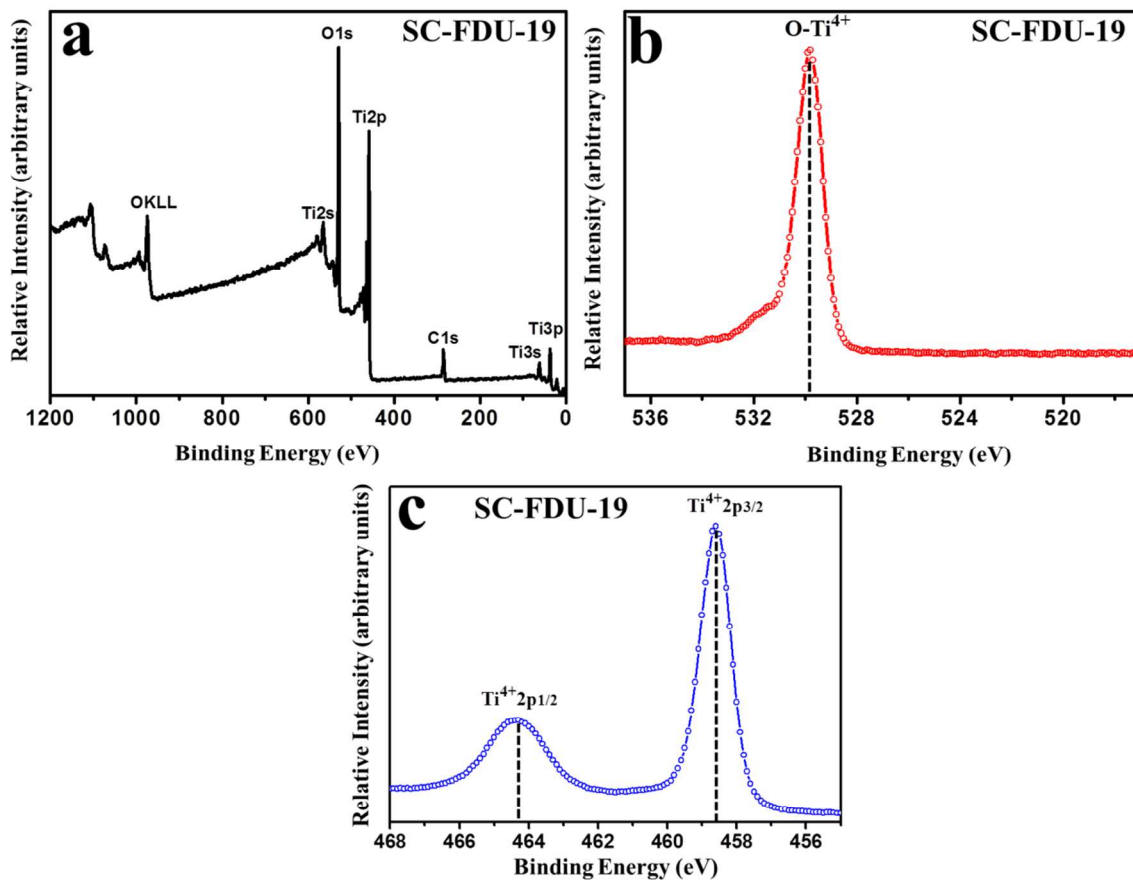


Figure S10. (a) The X-ray photoelectron spectra (XPS) of the mesoporous TiO₂ single-crystals SC-FDU-19, showing two characteristic peaks of Ti and O; (b) O1s XPS core-level spectra for SC-FDU-19. (c) Ti 2p XPS core-level spectra for SC-FDU-19.

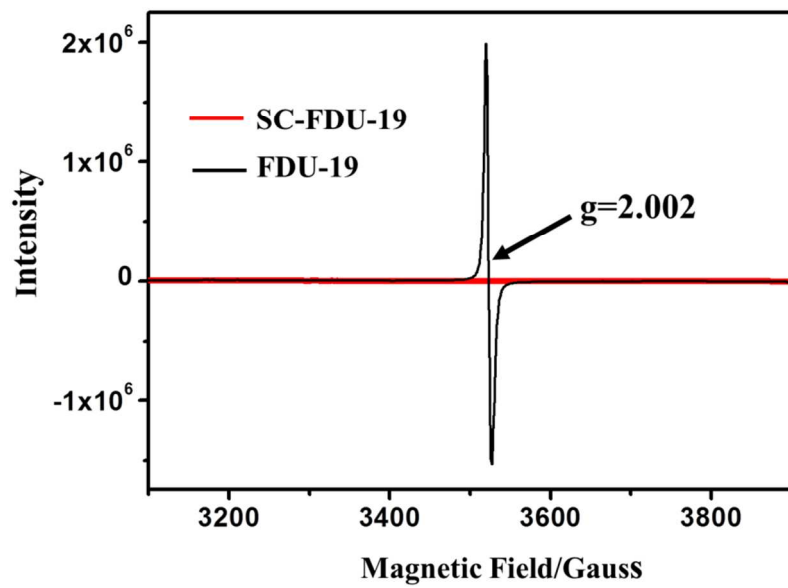


Figure S11. The electron paramagnetic resonance (EPR) spectra of the mesoporous TiO_2 mesocrystals FUD-19 and mesoporous TiO_2 single-crystals SC-FDU-19. The spectra are recorded at room temperature (25 °C).

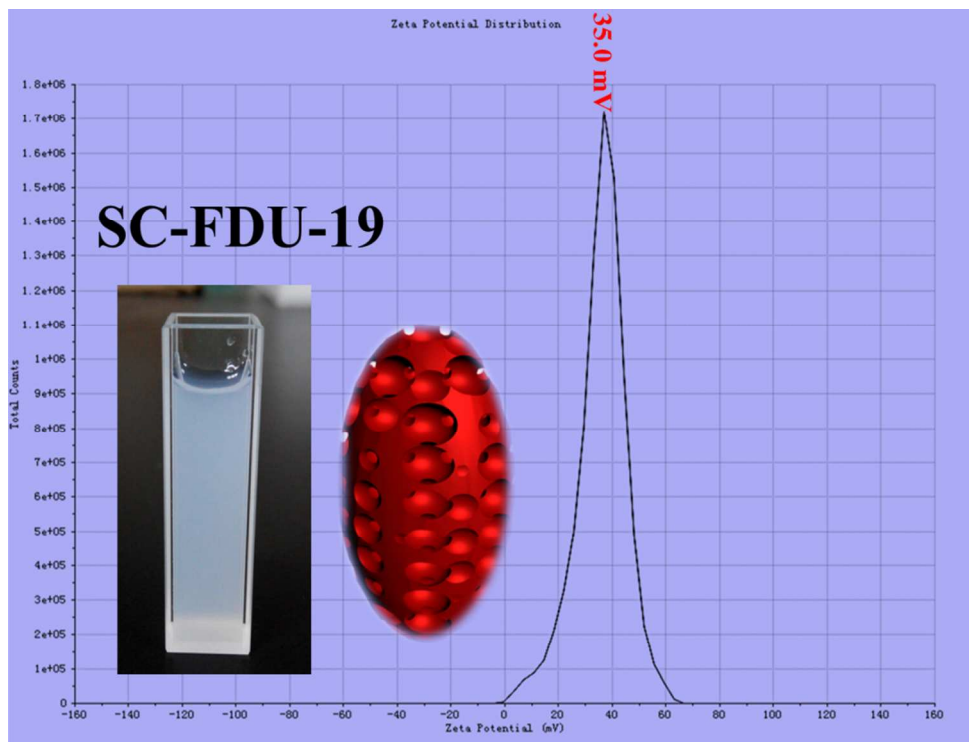


Figure S12. Zeta potential values (ζ) of the mesoporous TiO₂ single-crystals SC-FDU-19 dispersed in water as shown in inset, revealing that all the charges are positive.

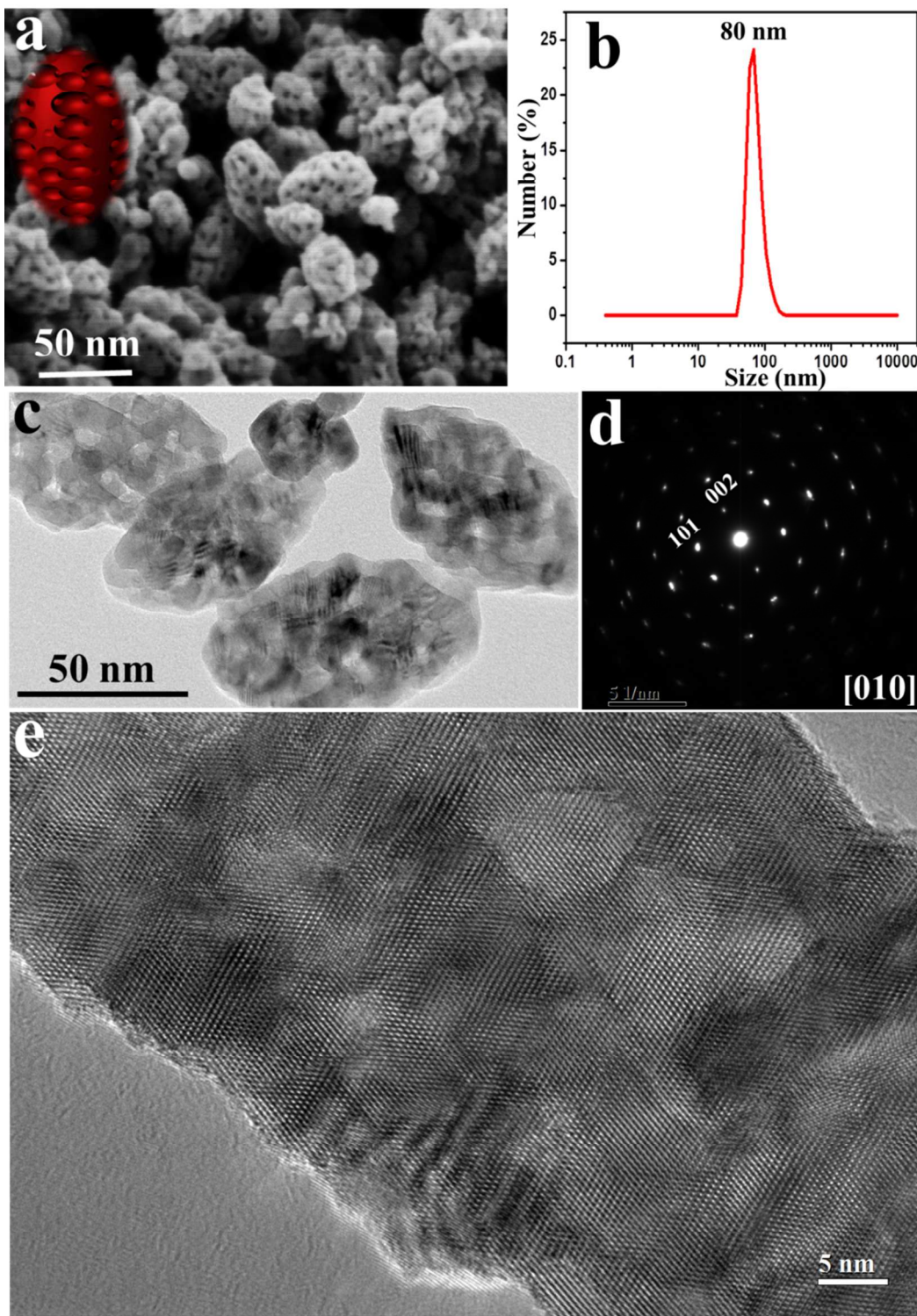


Figure S13. (a) The typical SEM image, (b) dynamic light scattering (DLS) spectrum, (c) TEM image of the mesoporous TiO_2 particles SC-FDU-19 with an average size of ~ 80 nm; (d) SAED patterns, (e) HRTEM image of a single particle SC-FDU-19 with a size of ~ 80 nm recorded along [010] axis.

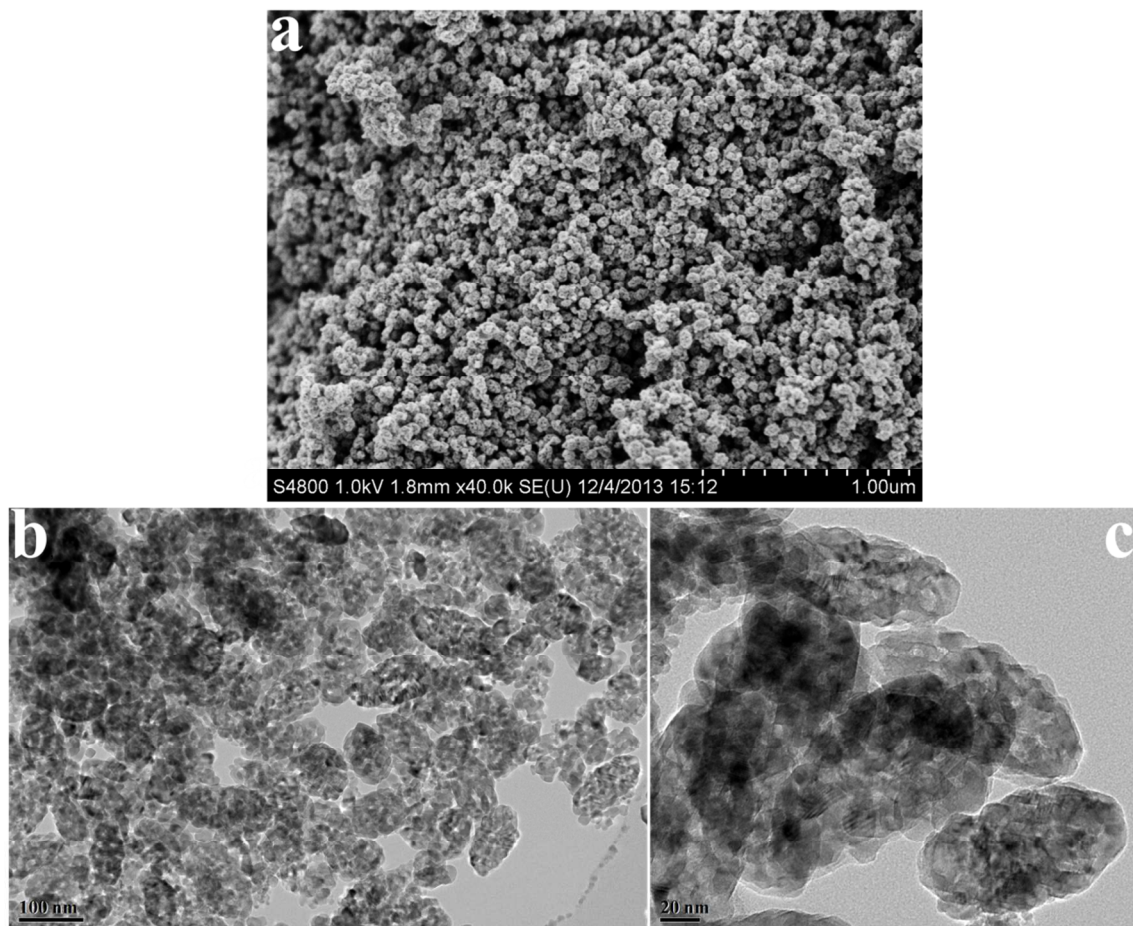


Figure S14. SEM (a) and TEM (b, c) images of the mesoporous TiO_2 single-crystal particles SC-FDU-19 with an average size of ~ 100 nm.

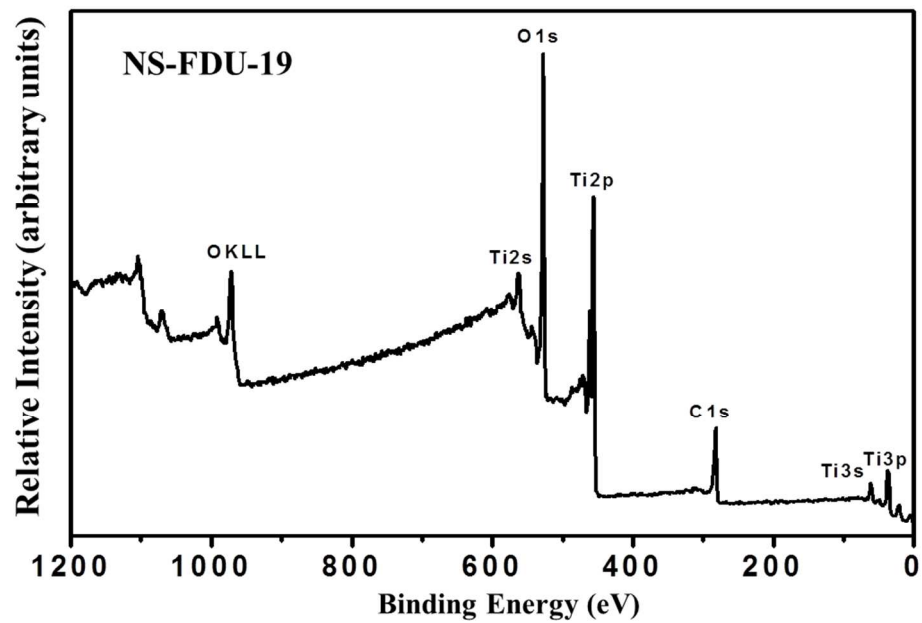


Figure S15. The XPS spectrum of the single-crystal TiO_2 nanosheets NS-FDU-19.

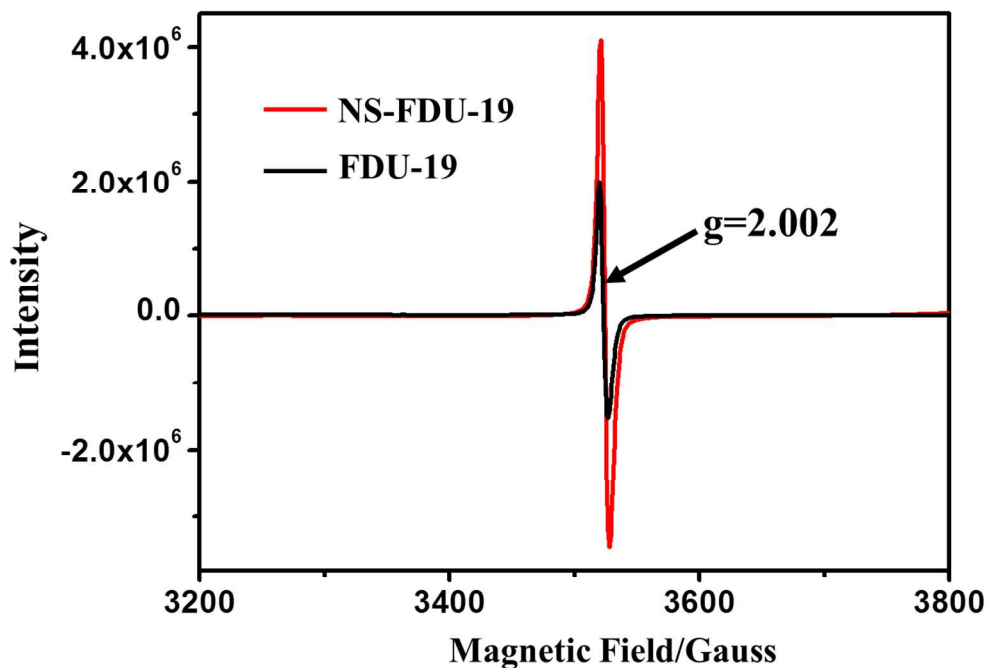


Figure S16. The electron paramagnetic resonance (EPR) spectra of the mesoporous TiO_2 mesocrystals FUD-19 and mesoporous TiO_2 single-crystals NS-FDU-19. The spectra are recorded at room temperature (25 °C).

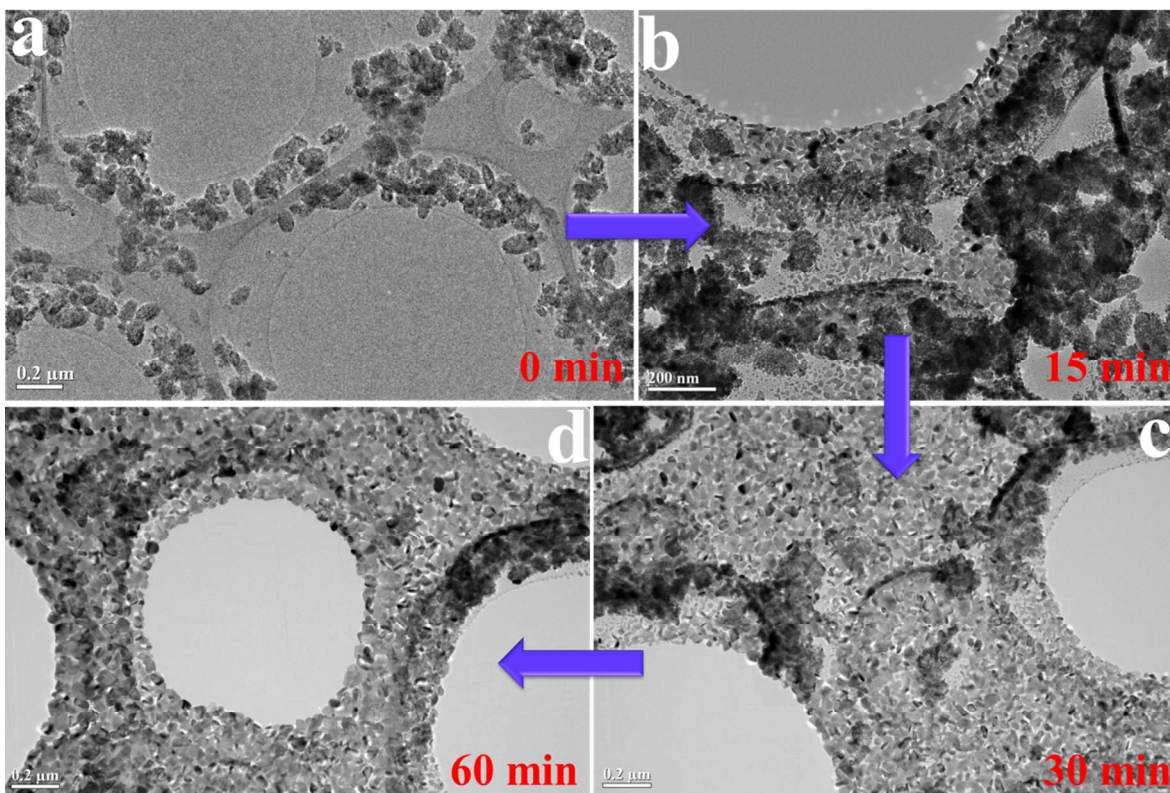


Figure S17. The *in-situ* TEM images of intermediates for NS-FDU-19 harvested at different intervals of time (a), 0 min, (b), 15 min, (c), 30 min and (d), 60 min. The *in-situ* TEM heating experiment was carried out at 400 °C in a high vacuum ($\sim 4.0 \times 10^{-5}$ Pa) on a grid with molybdenum supporting film using the EM-21130 Specimen Heating Holder.

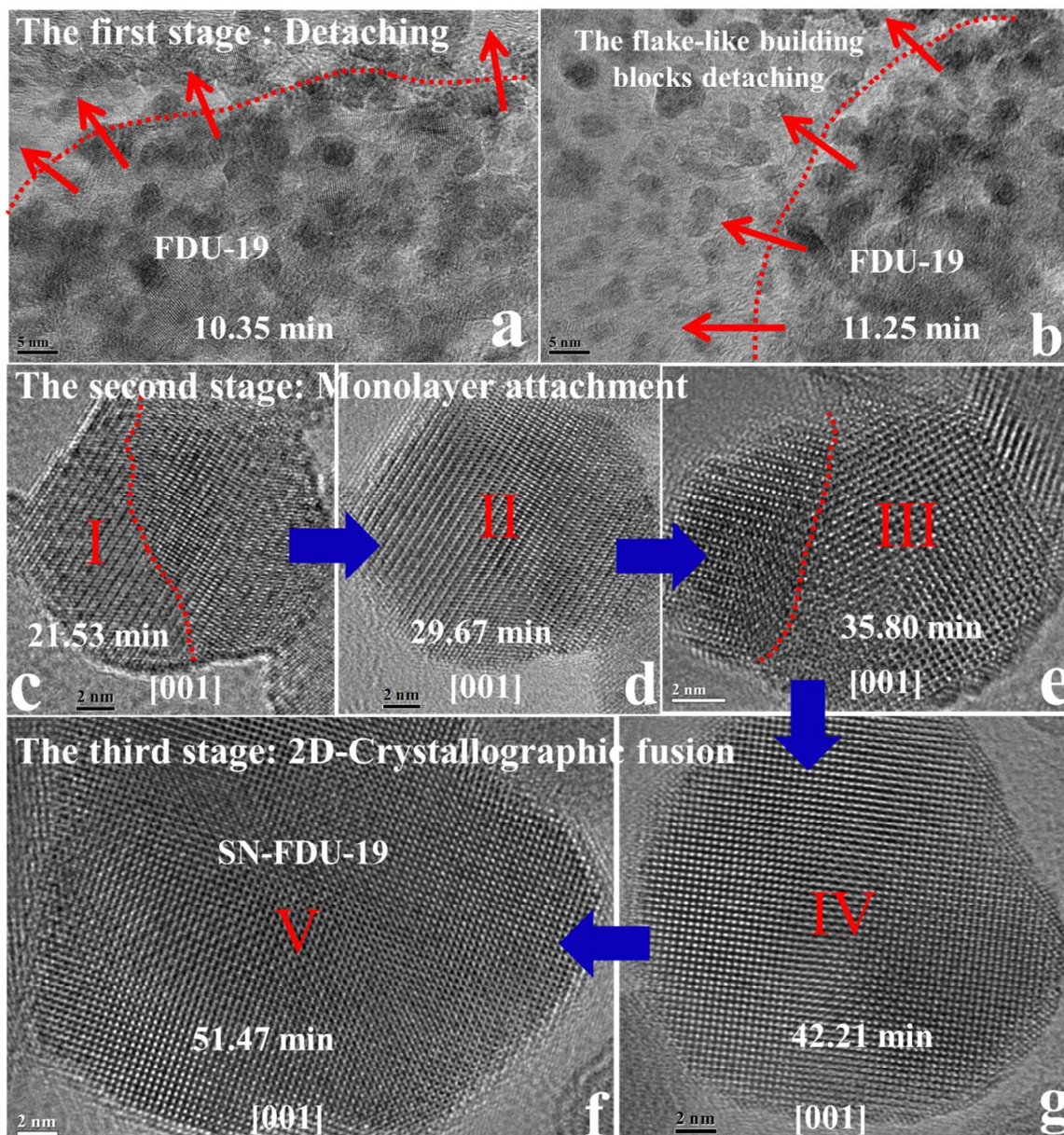


Figure S18. The *in-situ* HRTEM images of intermediates for SN-FDU-19 harvested at different intervals of time. The above *in-situ* HRTEM results obviously reveal that the growth of the ultrathin nanosheets NS-FDU-19 dramatically undergoes three stages: (i) the detaching of the flake-like nanocrystal building blocks from the mother FDU-19 mesocrystals (**a-b**); (ii) the continuous diffusion and rotation of flake-like nanocrystal building blocks for a monolayer particle attachment (**c-e**) because of the anisotropic electrostatic repulsion and dipole moments between the adjacent flake-like nanocrystal building blocks; (iii) the 2D complete crystallographic fusion of the nanocrystal building blocks to form an ultrathin single-crystal SN-FDU-19 nanosheet (**f-g**).

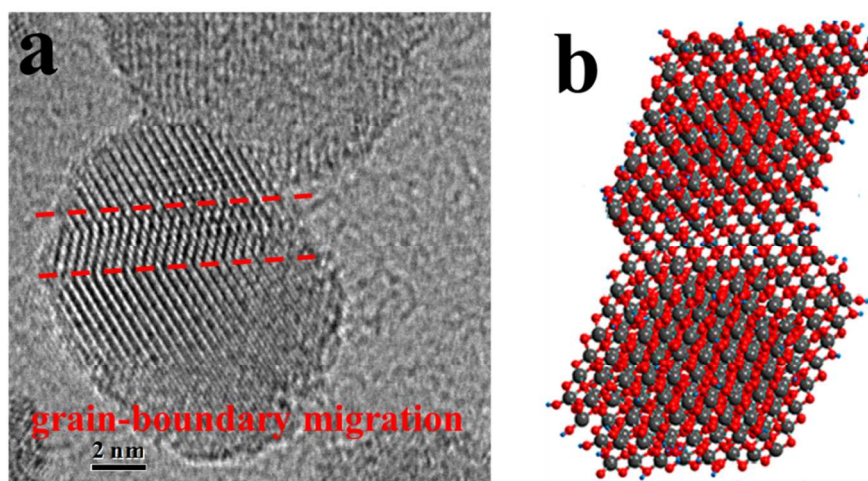


Figure S19. (a) The *in-situ* HRTEM image of an intermediate during the formation of NS-FDU-19 nanosheets harvested at 25.17 min. (b) The corresponding crystallographic simulation, showing that the monolayer-reconstruction undergoes an atom-by-atom reorientation *via* grain-boundary migration.

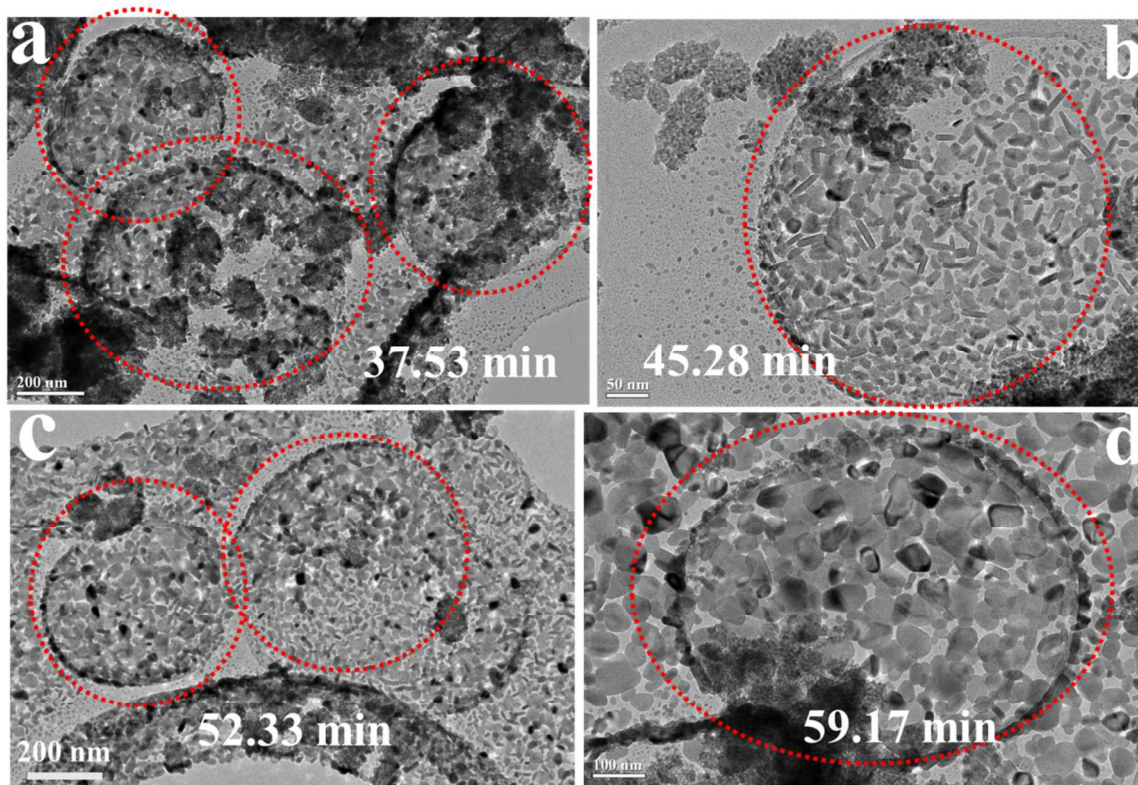


Figure S20. (a-d) The *in-situ* TEM images of the TiO₂ nanosheets NS-FDU-19 harvested at different intervals of time, showing that the freshly-formed SN-FDU-19 nanosheets are free-standing on the TEM grids with molybdenum supporting film in a spherical symmetry.

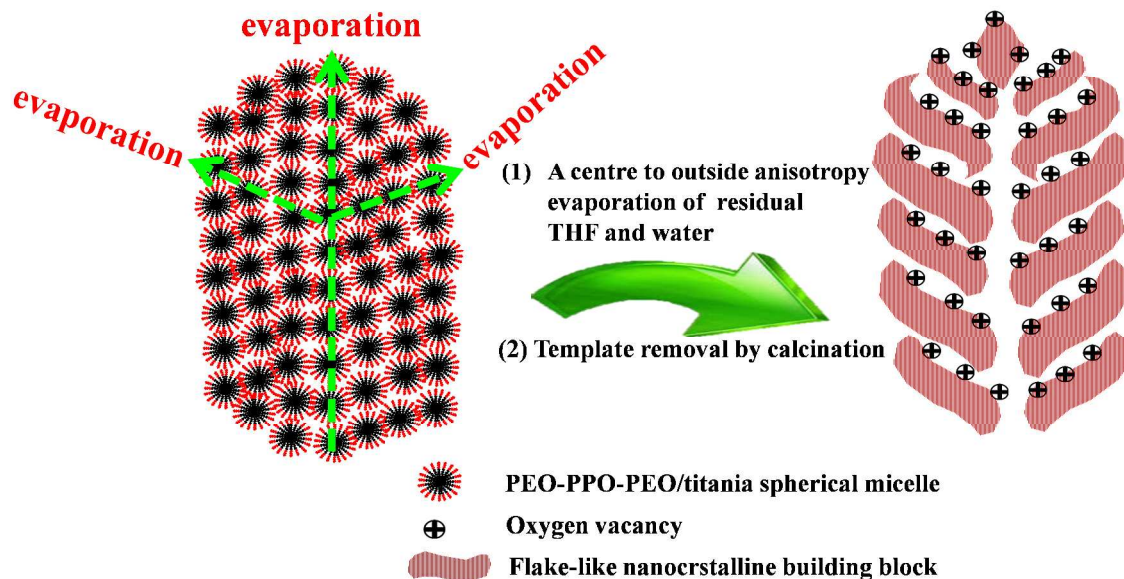


Figure S21. Schematic representation of the formation process of curving cylindrical channels within the olive-like mesoporous TiO_2 mesocrystals through the evaporation-driven oriented assembly process.

The high-boiling-point water is preferably evaporated up, which makes a slow driving force along c -axis, resulting in olive-shaped micelle aggregates. Finally, a centre to outside evaporation of residual THF and water can cause fusing PEO-PPO-PEO/titania spherical micelles into curving channel-like micelles along free radial and restricted tangential direction. Correspondingly, such a centre to outside evaporation force also drives TiO_2 oligomers cross-linked into flake-like nanocrystalline building blocks around F127 cylindrical micelles at a low temperature.

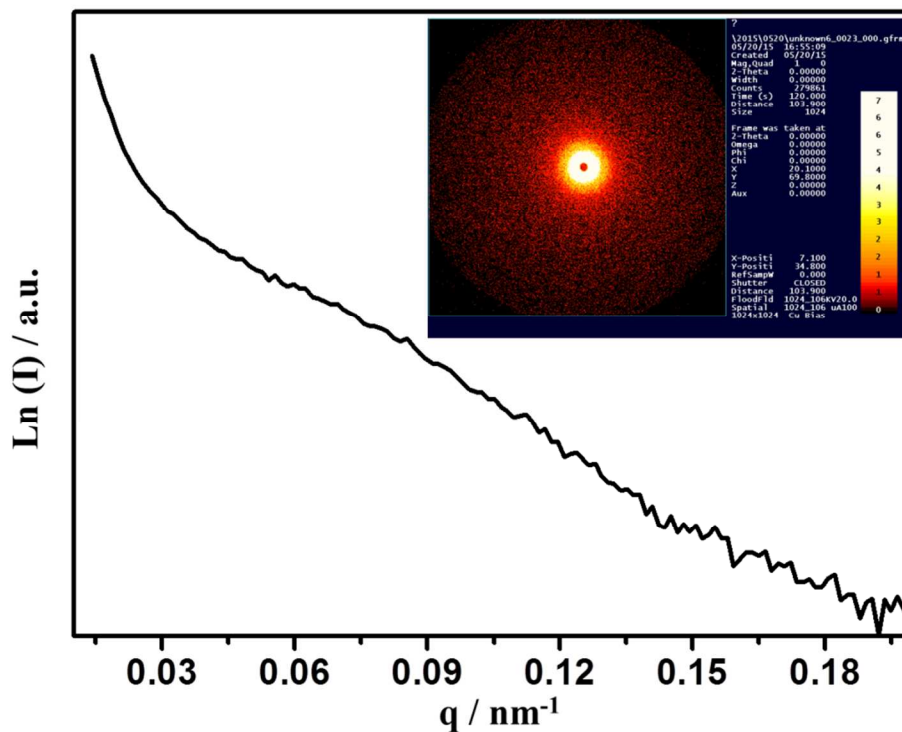


Figure S22. The small-angle X-ray scattering (SAXS) pattern of the as-made FDU-19. Inset is the corresponding 2D SAXS image of the as-made FDU-19.

A centre to outside evaporation of residual THF and water can cause fusing PEO-PPO-PEO/titania spherical micelles into curving channel-like micelles along free radial and restricted tangential direction, which is revealed by the degraded and broad scattering peaks for the as-made FDU-19

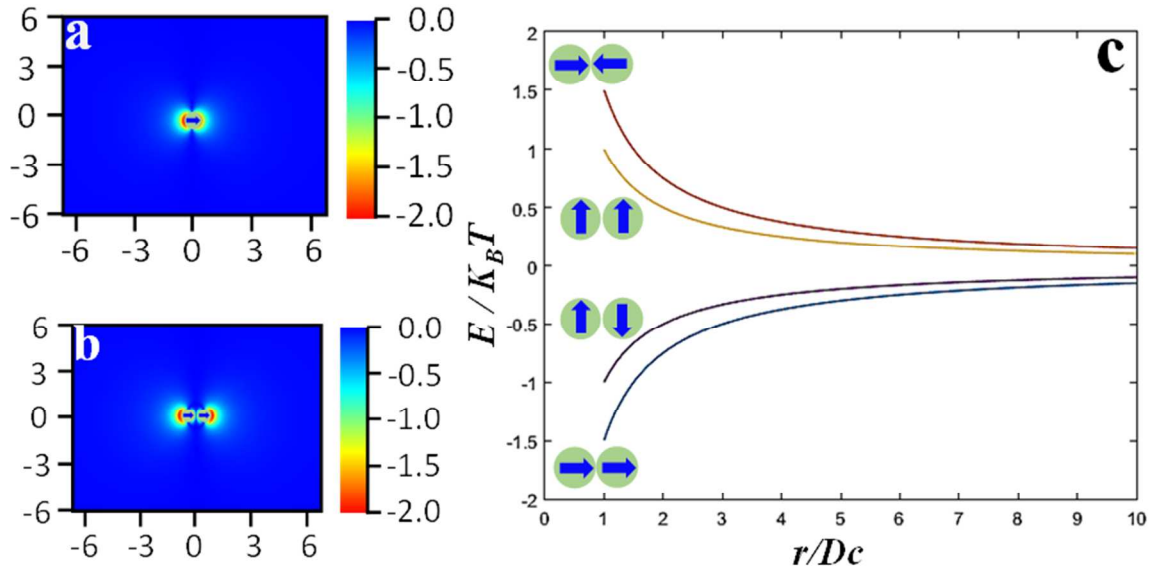


Figure S23. (a, b) Contour maps of the minimum electrostatic interaction energy exerted by a flake-like TiO_2 nanoparticle as another flake-like nanoparticle is approaching (a unit of $E/k_B T$ has been used, where k_B is Boltzmann's constant). (c), The electrostatic interaction energy as a function of inter-particle distance. Each flake-like nanoparticle is assumed to be a point electronic dipole. It illustrates that our observation of flake-like nanoparticle building blocks prefer to attach in 2D side-side monolayer alignment, rather than 3D bottom-bottom or bottom-side aggregations.

We assume the nanoparticles as volume-excluding sphere with point electric dipoles at their centers and calculate the electrostatic dipole-dipole interaction.¹ The nanocrystals internal structure, e.g., local variations of dipole density, crystal structure, length of ligands on the surface, *etc.*, is neglected. We calculate the electric potential energy of the interaction between two nanoparticles. We use the simple potential energy:^{1,2} $\beta u_{ij}^{dipole} = \frac{\lambda}{r_{ij}^3} \vec{e}_i \cdot [\mathbf{I} - 3\vec{r}_{ij}\vec{r}_{ij}] \cdot \vec{e}_j$ to represent the electrostatic interactions between two particles i and j , whose dipoles are oriented along the unit vectors \vec{e}_i and \vec{e}_j , respectively. The unit vector \vec{r}_{ij} points from i to j , and \mathbf{I} denotes the unit tensor. We express all distances in units of D_c , i.e., the diameter of a particle electric core is the distance between the centers of particle i to j relative to D_c . λ is a dimensionless measure of dipole-dipole interaction strength, we use $k_B T = 1/\beta$ as a unit of energy, yielding $\lambda = e^2/(4\pi\epsilon_0 D_c^3 k_B T)$, e is the magnitude of a particle's net electric dipole moment.

Table S1. Summary of other TiO₂-based DSSCs reported previously and their corresponding performance

Photoanodes	DSSC performance	Refs
Single-crystalline-like TiO ₂ mesocrystals	$\eta = 8.10\%$; $J_{sc} = 16.60 \text{ mA cm}^{-2}$; $V_{oc} = 0.748 \text{ V}$, FF = 0.65	(3)
Mesoporous TiO ₂ single crystals	$\eta = 7.29\%$; $J_{sc} = 12.86 \text{ mA cm}^{-2}$; $V_{oc} = 0.790 \text{ V}$, FF = 0.70	(4)
Single-crystal-like TiO ₂ nanowire	$\eta = 9.33\%$; $J_{sc} = 19.22 \text{ mA cm}^{-2}$; $V_{oc} = 0.720 \text{ V}$, FF = 0.67	(5)
Multilayered hyperbranched TiO ₂	$\eta = 11.01\%$; $J_{sc} = 18.53 \text{ mA cm}^{-2}$; $V_{oc} = 0.827 \text{ V}$, FF = 0.72	(6)
Anatase TiO ₂ nanospindles	$\eta = 8.30\%$; $J_{sc} = 16.40 \text{ mA cm}^{-2}$; $V_{oc} = 0.760 \text{ V}$, FF = 0.66	(7)
Tri-functional hierarchical TiO ₂ spheres	$\eta = 10.34\%$; $J_{sc} = 18.78 \text{ mA cm}^{-2}$; $V_{oc} = 0.826 \text{ V}$, FF = 0.67	(8)

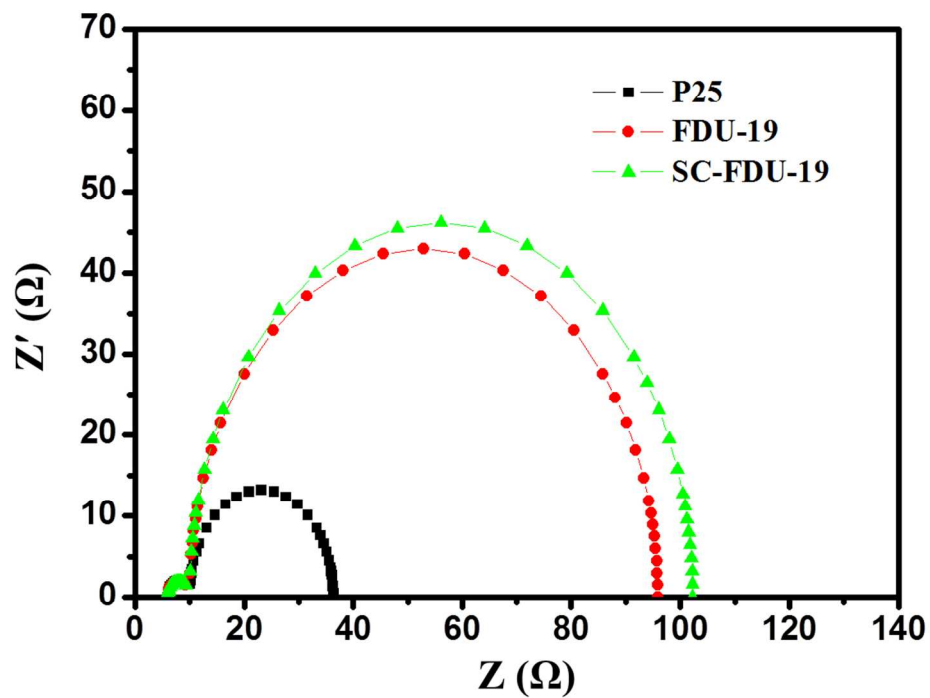


Figure S24. Nyquist plots of FDU-19, SC-FDU-19 and P25-based DSSCs (with the same photoanode film thickness of about 13 μm) measured at -0.8 V forward bias in dark.

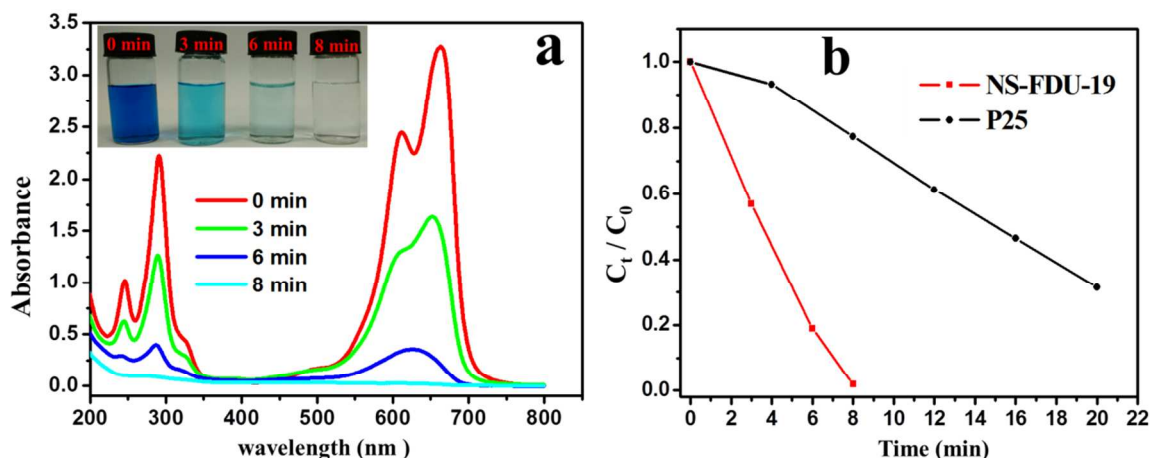


Figure S25. Photocatalytic decomposition of methylene blue dye (1.0×10^{-4} mol L⁻¹, 50 ml) over the TiO₂ single-crystal nanosheets NS-FDU-19 and Degussa TiO₂ P25. **(a)** UV-vis absorption spectra and corresponding color changes of the methylene blue solution (inset). **(b)** C_t/C₀ vs time curves of methylene blue photodegradation over NS-FDU-19 and Degussa P25.

References

- (1) Liao, H. G.; Cui, L. K.; Whitlam, S.; Zheng, H. M. Real-Time Imaging of Pt₃Fe Nanorod Growth in Solution. *Science* **2012**, *336*, 1011-1014.
- (2) Cho, K.-S.; Talapin, D. V.; Gaschler, W.; Murray, C. B. Designing PbSe nanowires and nanorings through oriented attachment of nanoparticles. *J. Am. Chem. Soc.* **2005**, *127*, 7140-7147.
- (3) Wu, D.; Cao, K.; Wang, H.; Wang, F.; Gao, Z.; Xu, F.; Guo, Y.; Jiang, K. Tunable synthesis of single-crystalline-like TiO₂ mesocrystals and their application as effective scattering layer in dye-sensitized solar cells. *J. Colloid Interface Sci.* **2015**, *456*, 125-131.
- (4) Crossland, E. J.; Noel, N.; Sivaram, V.; Leijtens, T.; Alexander-Webber, J. A.; Snaith, H. J. Mesoporous TiO₂ single crystals delivering enhanced mobility and optoelectronic device performance. *Nature* **2013**, *495*, 215-219.
- (5) Adachi, M.; Murata, Y.; Takao, J.; Jiu, J. T.; Sakamoto, M.; Wang, F. M. Highly efficient dye-sensitized solar cells with a titania thin-film electrode composed of a network structure of single-crystal-like TiO₂ nanowires made by the "oriented attachment" mechanism. *J. Am. Chem. Soc.* **2004**, *126*, 14943-14949.

- (6) Wu, W.-Q.; Xu, Y.-F.; Rao, H.-S.; Su, C.-Y.; Kuang, D.-B. Multistack Integration of Three-Dimensional Hyperbranched Anatase Titania Architectures for High-Efficiency Dye-Sensitized Solar Cells. *J. Am. Chem. Soc.* **2014**, *136*, 6437-6445.
- (7) Qiu, Y.; Chen, W.; Yang, S. Double-Layered Photoanodes from Variable-Size Anatase TiO₂ Nanospindles: A Candidate for High-Efficiency Dye-Sensitized Solar Cells. *Angew. Chem. Int. Ed* **2010**, *49*, 3675-3679.
- (8) Liao, J.-Y.; Lei, B.-X.; Kuang, D.-B.; Su, C.-Y. Tri-functional hierarchical TiO₂ spheres consisting of anatase nanorods and nanoparticles for high efficiency dye-sensitized solar cells. *Energy Environ. Sci.* **2011**, *4*, 4079-4085.